Concurrent *in situ* ion irradiation transmission electron microscope

K. Hattar *, D.C. Bufford, D.L. Buller

Department of Radiation–Solid Interactions, Sandia National Laboratories, United States

ABSTRACT

An *in situ* ion irradiation transmission electron microscope has been developed and is operational at Sandia National Laboratories. This facility permits high spatial resolution, real time observation of electron transparent samples under ion irradiation, implantation, mechanical loading, corrosive environments, and combinations thereof. This includes the simultaneous implantation of low-energy gas ions (0.8–30 keV) during high-energy heavy ion irradiation (0.8–48 MeV). Initial results in polycrystalline gold foils are provided to demonstrate the range of capabilities.

© 2014 The Authors. Published by Elsevier B.V. This is an open access article under the CC BY license (http://creativecommons.org/licenses/by/3.0/).

1. Introduction

The transmission electron microscope (TEM) has the well-known capability to observe specimens in real time at the nanoscale. Experiments performed *in situ* inside of the TEM provide the perfect platform for elucidating fundamental mechanisms governing material evolution in controlled environments. The knowledge gained from these experiments is essential to advancing predictive models of material response [1,2], which are important when traditional materials reliability testing cannot be performed either due to the remoteness of the application, harshness of the environment, longevity of service, or combinations thereof. Radiation environments pose substantial challenges due to obvious difficulties in performing experiments within high radiation areas, handling potentially radioactive materials, and with respect to the extended time often required for some effects to manifest.

In extreme circumstances, including space applications and nuclear reactors, the difficulties in predicting material response are exacerbated due to the often synergistic interactions that occur between various elements in the environment. This is seen firsthand in boiling water reactors, where radiation induced segregation can affect grain boundaries and interfaces in metal alloys, and shadow corrosion can affect dissimilar metals in close proximity [3,4]. Synergistic effects often manifest themselves when otherwise well-designed and controlled experiments exclude part of the radiation, stress, or corrosive environment. Tanaka et al. demonstrated minimal swelling in Fe–Cr alloys when irradiated with concurrent Fe/He and Fe/H beams, but more than one order of magnitude increase in swelling and void formation during irradiation with all three species at once [5]. In a similar fashion, due to the increased reliance on satellite based technology it has become essential to be able to predict device performance and thus materials properties in the radiation environment of space. Near-Earth space environments include a spectrum of energetic particles, which varies with distance and position relative to the planet. In addition to ions trapped by the magnetosphere, satellites are subjected to cosmic rays originating from the sun or other galactic sources. Microelectronic devices in these environments are not serviceable, and face degradation in performance and operation because of radiation damage events [6,7]. For all of these environments and many more, a fundamental experimental understanding of the evolution at the nanoscale, for which *in situ* TEM is ideally suited, is essential to validate and inform predictive models.

Not long after the invention of the TEM by Ruska in 1933 [8] and its commercialization in 1939 [9,10], several serendipitous observations of structural evolution dawned the beginning of *in situ* TEM experiments. These ranged from serendipitous ion implantation of the TEM foil in 1961 with oxygen from a contaminated tungsten filament [11], to observations of dislocation formation from displacement by energetic electrons [12]. Since these initial observations, a significant concerted effort has been made in the field to introduce a range of environments and radiation conditions, as well as thermal, electrical, and mechanical loading in a

* Corresponding author. Tel.: +1 (505) 845 9859.
 E-mail address: khattar@sandia.gov (K. Hattar).

controlled manner to the TEM sample. This has predominately been accomplished through the advancement of TEM holder technology applicable to the now standard side entry port design [13].

Throughout the last several decades, extensive research efforts have been undertaken at several laboratories around the world in an effort to introduce controlled ion beams into TEMs. An excellent overview of the development of these facilities and details of the ones operational in 2009 can be found in Ref. [14]. Each of these large, complex facilities operates under different experimental parameters dictated by the TEM utilized, the ion accelerator(s) attached, and the ion beamline specifics. These facilities have provided a wealth of fundamental insight into radiation–solid interactions over the last half century [15–21]. Over the same time period, *in situ* TEM deformation and failure studies have become increasingly refined. Initial controlled straining experiments with a simple applied external load have progressed to quantitative *in situ* tensile, compression, and indentation experiments where the associated stress and strain or load and displacement of the sample can be directly correlated to the evolution of the material observed in real time. The observations made using these evolving techniques have provided fundamental insight into the active mechanisms governing the plasticity of structural metals [22–28]. Finally, recent advancements in microfabrication tolerances have permitted rapid advancements in environmental TEM, from low vapor pressure conditions induced within the column or via dedicated facilities requiring significant amounts of differential pumping [29–32], to self-contained miniaturized environmental cells sealed by mechanically stable, electron transparent, amorphous membranes [33,34]. This recent advancement in vapor phase experiments now permits the incorporation of controlled liquid and gas environments into almost any TEM system.

Additionally, recent advancements in cathodoluminescence and electron tomography have been significant. *In situ* TEM cathodoluminescence is a technique that permits direct real time measurement of photons emitted from the material, as a result of the impinging electron beam. The collection efficiency of the technique has greatly advanced and now permits direct correlation between individual lattice defects and the resulting spectra [35]. Three-dimensional visualization techniques have seen rapid evolution due to significant computational advancements. In the past decade stereomicroscopy techniques have given way to full three-dimensional reconstructions that can be produced from automatically-collected tilting series [36], which permit a three-dimensional understanding of the material system. When performed sequentially with various *in situ* TEM techniques, a full four-dimensional understanding of the material's evolution is possible. Other advancements in traditional analytical TEM techniques outside of the scope of this manuscript have been recently reviewed here: [37,38]. The combination of these advancements permits the further development of complex *in situ* TEM experiments that can be run in overlapping extreme conditions not previously possible, with simultaneous potential for a greater wealth of experimental details to be obtained, analyzed, and incorporated into predictive models [39].

2. The instruments comprising the I³TEM facility

In order to better understand the fundamental mechanisms governing microstructural evolution in a range and combination of extreme environments, Sandia National Laboratories has developed a concurrent *in situ* ion irradiation TEM (I³TEM). This facility is housed within the Ion Beam Laboratory, a Sandia collaborative facility with a range of advanced ion beam capabilities [40,41]. The major components of the I³TEM facility can be seen in Fig. 1, and include a 200 kV JEOL 2100(HT) TEM, a 6 MV EN Tandem Van de Graaff–Pelletron accelerator, and a 10 kV Colutron G-1 ion accelerator. The JEOL 2100(HT) LaB$_6$ microscope, Fig. 1A, was chosen as it provides a versatile platform with a high tilt pole piece best suited for the high contrast imaging that is most beneficial for resolving radiation damage. The microscope was located within 1 cm and 1° precision during installation, providing the Tandem beam a direct path to the sample with minimal steering. This TEM has been outfitted with a TVIPS 4k × 4k camera that permits high quality single electron sensitive images and a 1k × 1k retractable camera that permits acquisition of video at up to 30 frames per second (FPS) during the *in situ* TEM experiments.

To maximize the resolution and stability of the TEM, an effort was made to minimize noise from electrical, mechanical, and thermal sources surrounding the instrument before connecting the ion beamline. As such, the facility utilizes high quality electrical power and dedicated grounds. The portion of the building housing the TEM was built to meet the VC-E vibration criterion of 3.12 μm/s, and its foundation is separated from the rest of the building by an isolation joint. The TEM area is isolated from the rest of the Tandem hall by heavy coated fabric laser curtains, which provide both noise and light reduction needed during experiments, while allowing easy access to the enclosed TEM and beamline components for operation and maintenance. HVAC vents in this area were equipped with radial flow diffusers, which provide low velocity high volume airflow, minimizing vibration while still allowing consistent temperature control. In addition, the standard passive pneumatic dampeners for the JEOL 2100 column were replaced with active vibration isolators, which better dampen low frequency vibrations around 1 Hz inherently associated with the column. Finally, the goniometer with piezo-controlled elements provides movement precision of up to 0.4 Å/step and factory-specified drift rate of 0.2 nm/min, permitting direct, relatively seamless corrections for the small drift typically experienced during many *in situ* TEM experiments. The combination of these efforts resulted in a TEM that maintains a 2.5 Å point resolution during most *in situ* ion irradiation and implantation conditions.

The 6 MV Tandem and 10 kV Colutron are connected to the I³TEM perpendicularly to the electron beam through a custom made electrically isolated and mechanically dampened port to ensure the highest resolution possible during *in situ* TEM experiments. The EN Tandem, Fig. 1B, originally manufactured in 1962, has been upgraded to use two Pelletron chains, Dowlish inclined field tubes, and a state of the art LabVIEW control system. The four ion sources available to the Tandem include SNICS (source of negative ions by cesium sputtering), Alphatross (rubidium exchange source for He⁻), a duoplasmatron proton source (for negative ions of gas atoms), and an Hiconex 834 sputter source where negative ion species can be quickly changed. The combination of sources permits the acceleration of a wide range of ion species ranging between protons and Au with energies as low as 800 keV and as high as 88 MeV, respectively. Beams are produced with controlled ion fluxes ranging from 1.6×10^7 to 3.2×10^{13} ions cm^{-2} s^{-1} incident on the sample. Greater details of the ion beam conditions previously run in this Tandem accelerator can be found in Middleton's cookbook [42].

Similarly, the 10 kV Colutron G-1 (Fig. 1C) was produced in 1979 [43,44], but was extensively retrofitted with new power supplies, vacuum system, and LabVIEW based control system during installation in the I³TEM facility. The Colutron can accelerate gas ions produced by a hot filament source to energies between 0.8 keV and 30 keV. Details on the various gas phases that have been accelerated out of similar Colutron guns can be found in these Refs. [45,46]. The upgrades to both accelerators have significantly increased the control and stability of the ion beams produced. In order to adequately manipulate the ion beams from both the Tandem and Colutron accelerators, a total of three quadrupole focusing magnets, two Einzel focusing lenses, five steering
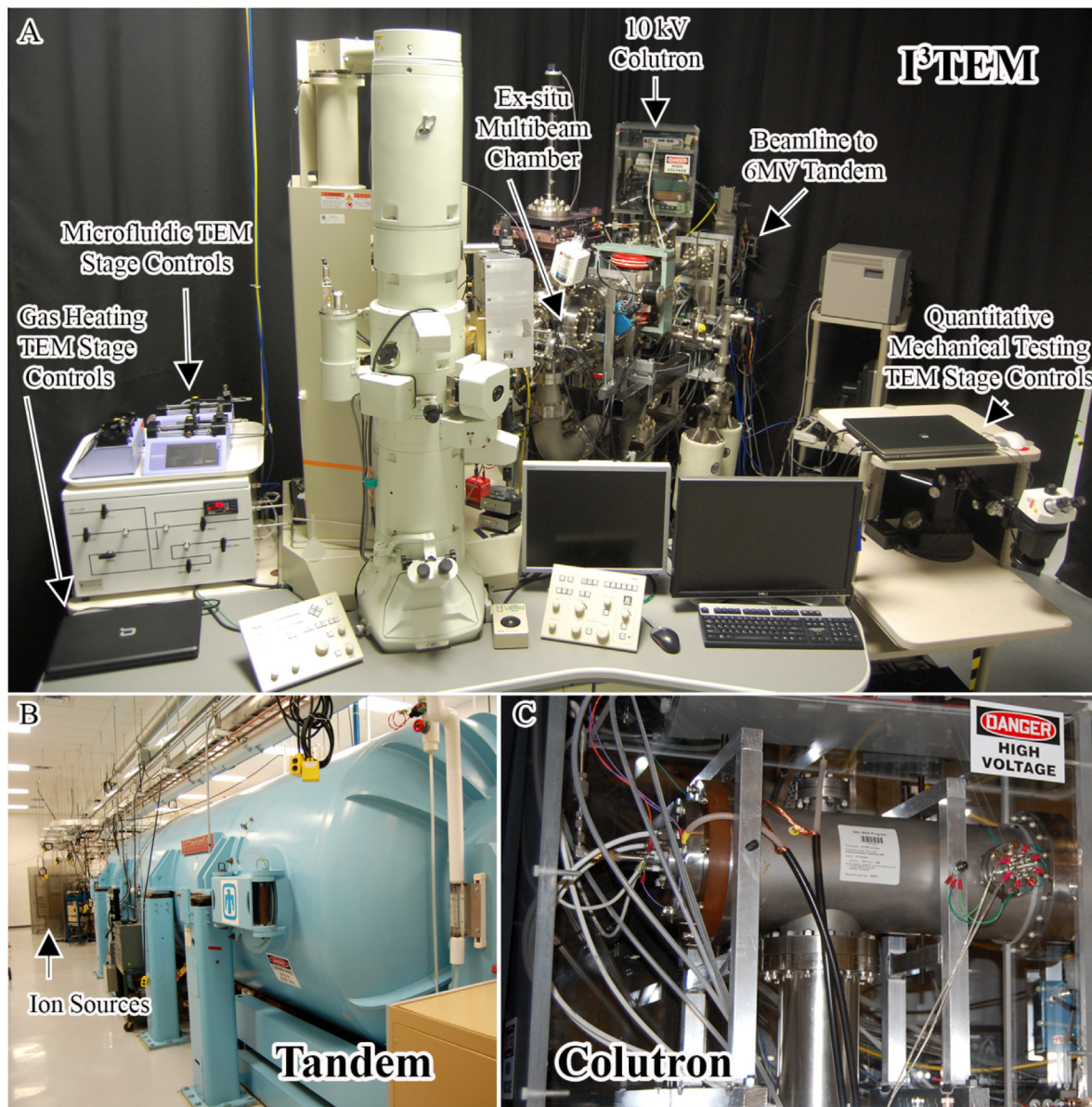
Fig. 1. I³TEM facility (A) JEOL 2100 TEM with key beamline and stage capabilities identified. (B) 6 MV EN Tandem Accelerator with the location of the ion sources identified. (C) 10 kV Colutron.

magnets, two electrostatic steerers, and three dipole bending magnets are used between the ion sources and the TEM. In the same way, a set of four viewing screens, five Faraday cups, and three beam profile monitors is used to characterize both ion beams at several locations along the beamlines. The range and complexity of a portion of this ion beam system can be seen in the I³TEM beamline schematic shown in Fig. 2.

3. *Ex situ* dual beam capabilities

A significant concern with any *in situ* TEM experiment is determining the effects associated with TEM sample preparation, small sample dimensions, and electron beam irradiation of the sample. In order to address these concerns, an *ex situ* implantation chamber was incorporated less than 1 m upstream of the TEM, as shown in Fig. 1A. The chamber was placed as close to the TEM as was allowed by the physical connection and final ion beam characterization components. This arrangement permits validating electri-

cal, thermal, and small-scale mechanical testing experiments to be run on larger samples exposed to identical ion species, energies, and dose conditions as those observed during *in situ* TEM experiments. The chamber can expose sub-regions of samples up to 100 mm in diameter to any combination of ion beams that can be aligned into the TEM, including concurrent combinations of high-energy heavy ion beams from the Tandem accelerator and low-energy gas ion beams from the Colutron. The samples are positioned by a four-axis stage, and the chamber includes unused ports that ensure additional potential for expansion. A significant vacuum capacity including Venturi, cryosorption, and turbomolecular pumps permits independent venting and rapid pumping of the chamber during full isolated operation of the TEM, Colutron, and Tandem. The ability to perform dual beam experiments on regions of wafer-size samples provides both a unique capability to validate *in situ* TEM experiments and a means to provide deeper direct understanding into the property evolution that occurs in extreme radiation environments.
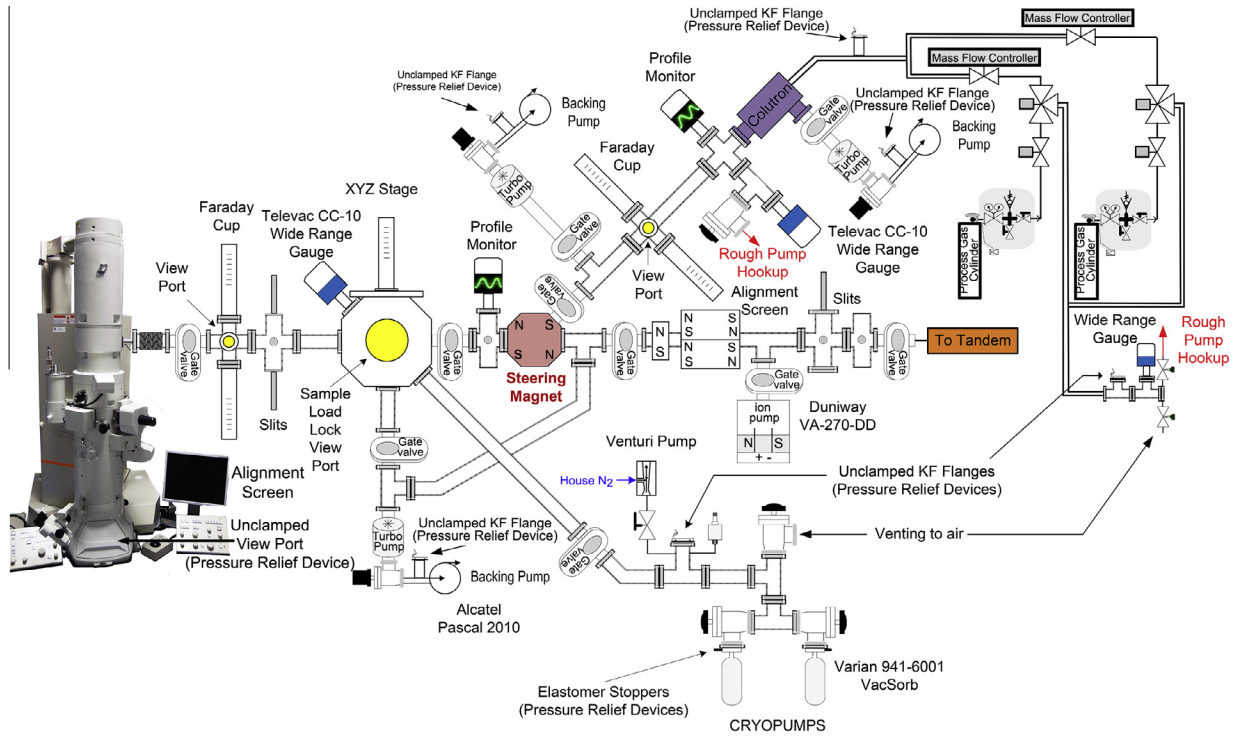
Fig. 2. Schematic of the I³TEM beamline including details of the vacuum system. The schematic excludes the Tandem accelerator and associated beamline components.

4. Ion beam conditions

The combination of the Tandem and Colutron accelerators provides a wide range of ion species and energies that can be run into the TEM. The ion beam species and energies that have been run into the TEM, as of July 2014, can be seen in Fig. 3. The Tandem accelerator has been used to introduce ion species into the TEM ranging from protons to Au at energy ranges from 800 keV to 48 MeV. As can be seen in Fig. 3, alpha particles from the Alphatross source (solid points) and a wide range of sputtered ions (open/crossed points) have been successfully inserted into the TEM. It should be noted that Tandem accelerators are not amenable to heavy noble gases, as the half-life of these negative ions is

substantially shorter than the time needed for the ion to travel through the accelerator. The dose rate achieved with each ion beam was found to be dependent on the sputter rate, beam rigidity, and the beam optics, as expected. The maximum ion energy and mass currently achievable in the TEM is limited to a beam rigidity of 35 MeV-amu-q^{-2} by the maximum magnetic fields of the beam steering components. Despite this limitation, ion beams of energies as high as 48 MeV Si^{8+} (21 MeV-amu-q^{-2}) and 14 MeV Au^{12+} (19 MeV-amu-q^{-2}) have been introduced into the TEM. Ion beams originating from the Tandem can be focused down to an approximately 3 mm diameter spot on the TEM stage or broadened to approximately 25 mm in diameter in the *ex situ* chamber. With a beam spot approximately 5 mm in diameter, ion fluxes ranging from 1.6×10^7 to 3.2×10^{13} ions cm^{-2} s^{-1} (computed from currents measured by a Faraday cup placed before the sample, and confirmed by a custom Faraday stage and by counting damage cascade events within a known field of view) have been achieved at the sample holder. Considering a 1 μm × 1 μm field of view, these fluxes correspond to one ion strike roughly every 6.3 s–3 μs, respectively. The Colutron accelerator can accelerate gas ion species between 0.8 keV and 30 keV, with a range of fluxes comparable to those from the Tandem. Since being attached to the TEM, it has been used to accelerate 5–10 keV He$^+$ and D$_2^+$, 20 keV He^{2+}, 10 keV Ne$^+$, and 20 keV Ne^{2+}. These experimental conditions also permit the study of a broad range of ion effects; three extreme cases highlighting this capability within Au films will be presented in Section 7:
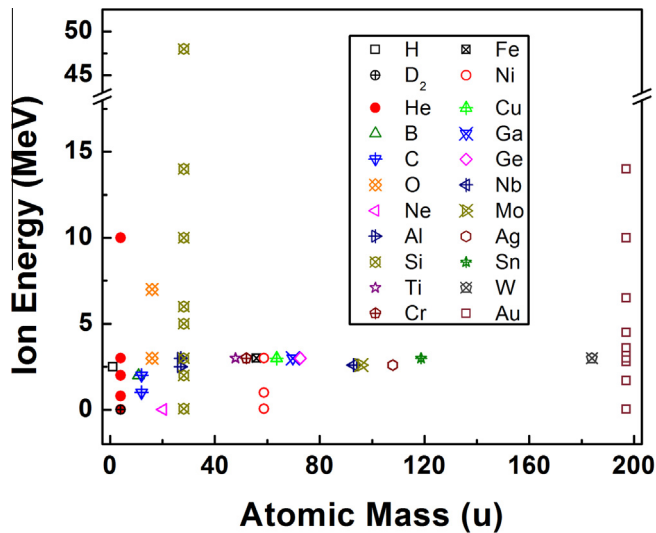
(1) Implantation with minimal displacement damage: TRIM calculations [47] predict an end of range of 35 nm for 5 keV D$^+$ with nearly 50% of the ions trapped in the 50 nm-thick Au foil, while creating 3 vacancies per ion.
(2) Significant and nearly uniform displacement damage: TRIM calculations predict an end of range of 240 nm for 3.6 MeV Au and approximately 4500 vacancies per ion produced in a 50 nm-thick Au foil with limited ions trapped.

Fig. 3. Masses and energies of ion species introduced into the I³TEM to date. Solid points denote protons and alpha particles from the Alphatross source, and open/crossed points indicate sputtered ions from the SNICS or gas ions from the Colutron.

(3) Significant electronic stopping with minimal nuclear stopping: TRIM simulations predict an end of range of 5.6 µm for 48 MeV Si and an average of approximately 21 vacancies per ion produced in a 50 nm Au foil, with essentially no ions stopped.

The feasibility of doing concurrent ion irradiation from the Tandem and ion implantation from the Colutron is limited by the difference in the beam rigidities, as the Colutron beam must be bent 20° without significant deflection of the Tandem beam, such that the two beams are collinear. For experiments involving low energy implanted ions and high energy heavy ions, the rigidity is often so different that the Colutron bending magnet barely affects the high energy ions. For example, the beam rigidity ratio between the 3.6 MeV Au^{6+} ions and 10 keV He^+ ions presented in this paper is nearly 500. Work is still under way to quantify the extent of rigidity difference needed for successful dual beam experiments. The range of ion species and ion energies that have been demonstrated to date permits an excellent test platform to study fundamental aspects of radiation damage evolution in materials.

In addition to the positive ions that can be directly obtained from the Tandem or Colutron accelerators, it has also been demonstrated that negative ions can be produced from the SNICS source and transported through the Tandem accelerator. Ion beams with energies ranging from 40 to 70 keV are achievable by taking the Tandem terminal up to as high as a few hundreds of kV but not introducing any stripper gas. The negative beam then accelerates towards the terminal in the low energy end of the tandem, but decelerates in the high energy end, and better transmission of these negative ions through the tandem is obtained. As a result, any ion species that can be sputtered at an appreciable current can be implanted into a TEM foil during real time nanoscale observations. This has been demonstrated with the introduction of 64 keV Si^-, 64 keV Ni^-, and 46 keV Au^- beams into the TEM.

5. I³TEM optics and control systems

5.1. Inclusion of photon optics

Although the I³TEM is not outfitted with common analytical additions, it was designed to incorporate optical pathways to the sample, which can be used either for the collection or introduction of light for use with various photon-based analytical techniques. In order to accommodate both electron and optical techniques, two ion optics, two photon optics, and an electron optics system all had to be aligned to a single 3 mm disk located within the TEM column. A schematic of this complex arrangement can be seen in Fig. 4A. In addition to the two ion beam paths into the TEM, the I³TEM also has two optical pathways. One of the ports utilizes a
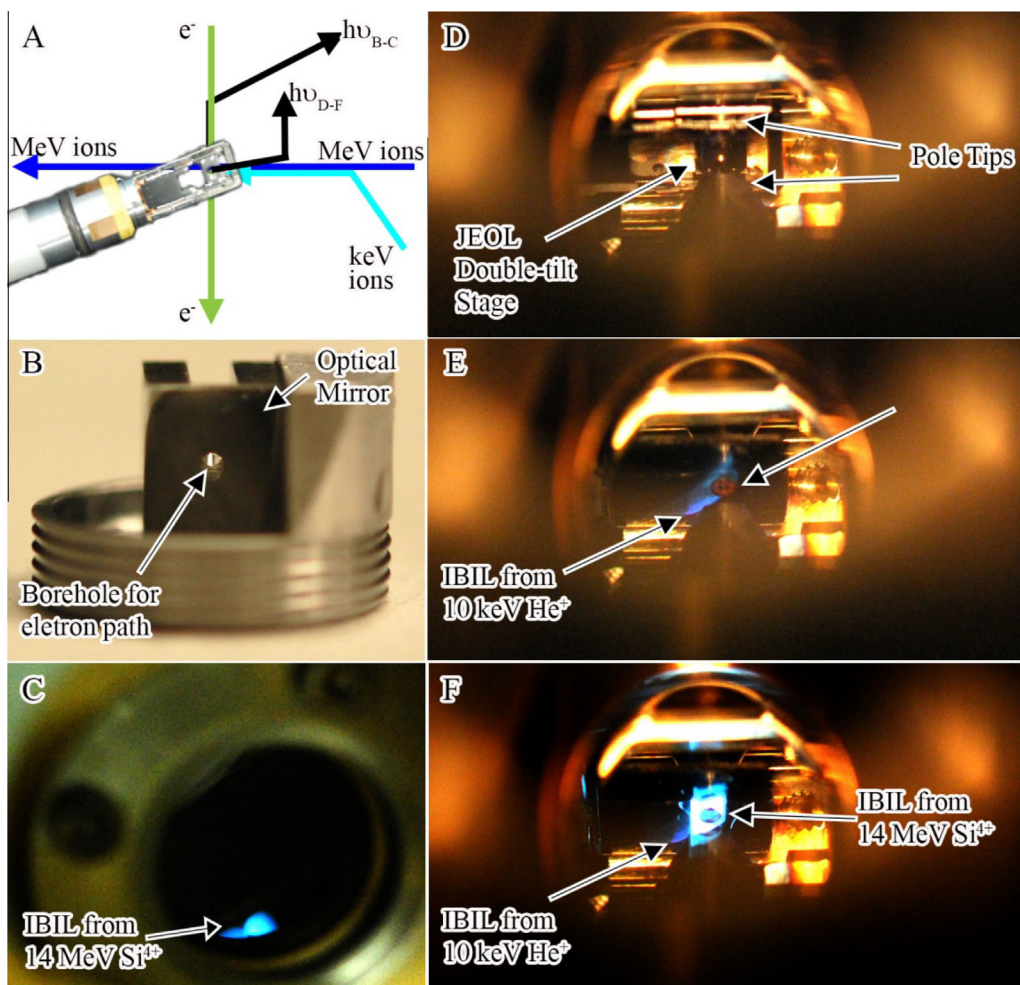

Fig. 4. (A) Schematic of the electron beam, high and low energy ion beams, as well as two photon optic pathways all aligned to the same 3 mm spot in the I³TEM. (B) Custom mirror piece above the TEM polepiece. (C) Ion Beam Induced Luminescence (IBIL) from 14 MeV Si^{4+} impacting a fused quartz slide on a custom TEM stage tip viewed from the top entry port. (D) JEOL double tilt stage loaded in the TEM through the ion beamline during TEM operation. (E) IBIL from 10 keV He^+ impacting a fused quartz TEM stage viewed through the ion beamline. (F) IBIL from 14 MeV Si^{4+} impacting a fused quartz TEM stage viewed through the ion beamline.

custom made metal mirror that screws directly into the upper pole piece plate. This mirror, with a borehole for the transmission of the electron beam (Fig. 4B), creates a light path from the TEM sample through the upper pole piece to the high angle EDS port of the JEOL 2100. The complex light path and high reflectivity of the required metal mirror limit light transmission, reducing its usefulness for optical imaging, as illustrated in Fig. 4C. However, it can still be used for illumination. The other optical port utilizes a tilted mirror located in the top fraction of the ion beam port, providing a much better low light image nearly in line with the perspective of the ion beam. Fig. 4D is an image of the JEOL double-tilt stage without a sample loaded and titled to 30° in α. The image is taken with a digital single-lens reflex (DSLR) camera using a microlens mounted externally to the beamline port. Within the port diameter, the details of the TEM objective lens and double-tilt stage can be seen, including the trapezoidal structures of the pole piece and the hole where the TEM sample is normally present in the double tilt stage.

Because both ports can be used for the insertion or collection of light, a wide set of well-developed techniques including: direct illumination, laser heating, ion beam induced luminescence (IBIL), cathodoluminescence (CL), or photoluminescence (PL) techniques are all feasible. The use of a custom made IBIL TEM stage permits rapid direct alignment of the ion beams on the TEM sample. In Fig. 4E, the illumination of an aligned 10 keV He$^+$ beam is seen on the stage. Similarly, IBIL from both a 10 keV He$^+$ beam and a 14 MeV Si^{4+} beam can be seen incident on the TEM sample. While MeV-range heavy ion beams were readily aligned to the sample, it was found that the low-energy, light-mass ion paths were significantly altered by the objective lens of the TEM. As such, the implantations of electron transparent foils can either be done with a direct beam with the TEM operated in low magnification mode (objective lens off) or in high magnification mode with the final electrostatic ion steerers located in the TEM connection used to compensate for the primary steering effects of the TEM objective lens on the light ions.

5.2. Monitoring and control systems

Modern ion accelerator and electron microscope control software enables fine monitoring and manipulation of the entire system. The JEOL 2100 TEM associated with the I^{3}TEM facility has an additional detached JUS-SERIUS, a JEOL remote control client, permitting completely integrated operation of the microscope from a safe working distance after the sample has been loaded. In a similar manner, the modern Tandem and Colutron LabVIEW control codes permit both accelerators to be aligned and operated remotely once the ion sources have been loaded and the start-up completed. This capability makes it possible to perform experiments that produce ionizing radiation external to the TEM, which would otherwise be impossible as the TEM area would be classified as a radiation or high radiation area during the experiments, for example, neutron-producing experiments involving bombardment of beryllium or deuterium-containing samples by energetic protons or alpha particles.

In addition to the ability to control the entire I^{3}TEM facility remotely, the modern accelerator control systems permit direct recording of many instrument and environmental parameters during the experiments. Two examples of recorded parameters important to the quality and stability of any TEM experiment can be seen in Fig. 5A and B. In Fig. 5A, the temperatures of two thermocouples are reported, one directly adhered to the outside of the JEOL 2100 objective lens and the other in the center of the I^{3}TEM curtained area. This information has already been utilized to modify the facility to minimize thermal drift during long in situ irradiation experiments, permitting overnight unattended observation of a single square micron region. The vacuum pressures of both the TEM
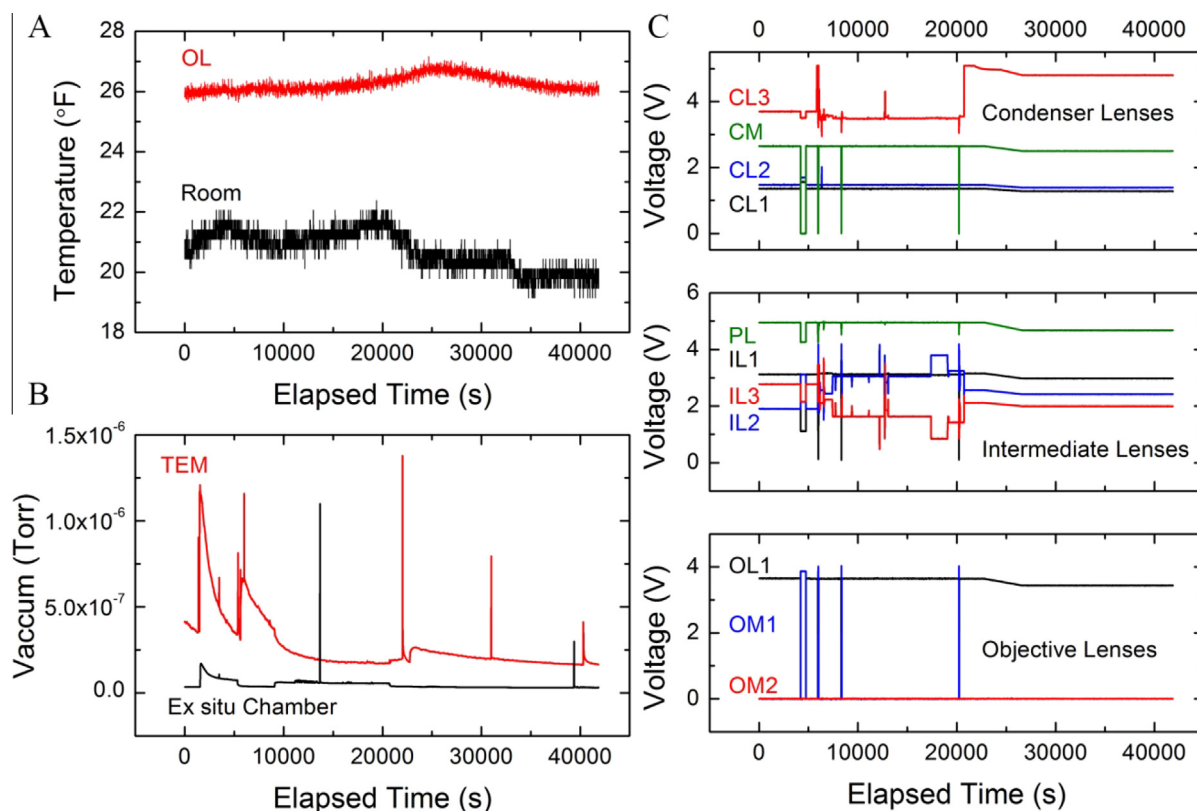

Fig. 5. Plots of TEM and beamline parameters during operation over a 12 h period. (A) Recorded temperature variations of the objective lens and the room. (B) Vacuum pressure of the TEM column's ion gauge and the dual beam chamber located within the I^{3}TEM beamline. (C) Measured voltages of all the JEOL 2100 TEM lenses.

column and *ex situ* dual beam chamber are also recorded, Fig. 5B, and have provided information utilized to identify and minimize small vacuum leaks in the system that developed over time. This has permitted the Tandem beamline, Colutron beamline, and TEM to regularly achieve a vacuum of 1×10^{-8} Torr. It should be noted that the *ex situ* dual beam chamber pressure is consistently better than the TEM pressure, providing additional pumping capacity to the TEM during operation. In addition, the JEOL 2100 has been modified following the technique developed by Mecklenburg in order to permit direct digital recording of the electromagnetic lens statuses within the TEM. An example of lens voltage during a 12 h period can be seen in Fig. 5C. In this figure, one can observe both the significant changes in lens voltage associated with changes in imaging mode or magnification. Insight from these settings verified that the objective lens (OL1) is the only lens that can alter the trajectory of the low-energy, light ion beams. The ability to monitor the TEM and accelerator parameters during experiments, as well as to directly record the parameter history of events, permits not only better maintenance and upgrades to the system, but greater efficiency of the research during complex *in situ* TEM experiments.

6. Combination of *in situ* conditions

In addition to the concurrent ion irradiation and implantation conditions that can be produced using the Tandem and Colutron, a variety of other combinations of *in situ* TEM capabilities are feasible utilizing the I³TEM. Despite the electron and ion optics being nearly normal to each other, a variety of commercial TEM stages associated with the facility have the tilt range to overcome the shadowing limitation of the stage. At the eucentric height, the standard JEOL single-tilt and double-tilt stages are exposed to both beams within the approximate ranges $-48°$ to $-23°$ and $+17°$ to $+47°$, the Gatan Faraday stage can be exposed to both beams over the range of $-82°$ to $-26°$ and $+26°$ to $+82°$. The *in situ* manipulation stages vary in their accessibility to the ion beams; the Protochips microfluidic and gas flow stages are exposed over respective tilt ranges of $+22°$ to $+27.5°$ and $-22°$ to $-27.5°$ after custom modifications, the Hummingbird 2.3 mm heating stage is exposed in the range of $+24°$ to $+42°$, the Hysitron PI 95 stage is accessible over the ranges of $-42°$ to $-12°$ and $+12°$ to $+42°$, while the Hummingbird single tilt tomography stage has no middle shadow resulting in a range of $-82°$ to $+82°$. It should be noted that none of these tilt ranges consider the potential shadowing from the TEM sample itself, as this may vary significantly.

The Protochips microfluidic and gas flow stages encase samples in sealed cells with SiN windows that permit gas or liquid flow inside of the TEM. With these cells it is possible to study samples in aqueous environments, ranging from biological structures [48] to metals undergoing corrosion. The gas flow cells also have heating capability, allowing studies of chemical processes like hydriding [49]. The modifications permitting the introduction of energetic ion into these environments have opened up a range of *in situ* environmental irradiation studies not previously possible. The combination of the Hummingbird heating stage with the facility permits ion irradiation or implantation experiments at temperatures up to 800 °C. By controlling the heating stage and Colutron from the same computer platform, synchronized data collection is possible, permitting direct comparison of the temperature changes to differences in the monitored TEM and Colutron variables. No current capabilities exist at this facility for *in situ* ion irradiation TEM experiments to be performed below room temperature. In a similar manner, the combination of the I³TEM facility with the Hysitron PI 95 TEM stage permits direct real time correlation between the quantitative nanoscale mechanical properties and

the associated structural evolution during mechanical loading. This stage directly allows indentation and compressive loading, as well as tensile loading by means of microfabricated "Push-to-Pull" test frames or custom fabricated grippers. Custom loading functions with respective maximum force and displacement of 1.5 mN and 5 μm can be constructed permitting a range of potential loading schemes including fatigue. Such experiments can be observed in real time at the nanoscale within the radiation environment permitted by the facility. Additionally, samples loaded into the PI 95 can be heated by means of a microfabricated heater, allowing measured temperatures up to 400 °C to be applied *in situ* concurrently with mechanical loading and ion irradiation. Because of recent advancements in TEM camera and data processing capabilities, it is possible to collect single electron sensitive diffraction patterns or serial tilt-series permitting three-dimensional reconstructions of the observed changes. By pausing *in situ* experiments at regular intervals and utilizing these capabilities time-resolved structural information can be obtained [50], greatly enhancing the understanding of the system under study.

7. Demonstration of I³TEM capabilities

The following section includes several demonstrations of the range capabilities of the I³TEM facility. Polycrystalline Au foils nominally 50 nm-thick were used as a model system in these experiments. These samples were deposited by pulsed laser deposition (PLD) onto NaCl substrates, then floated off in deionized water and collected on Mo TEM grids. Because PLD depositions typically result in nanocrystalline grain sizes and far from equilibrium microstructures [51], the samples were annealed in a vacuum furnace ($\leqslant 5 \times 10^{-6}$ Torr) at 300 °C for 12 h, and allowed to cool to nominally 50 °C before removal. The resulting samples had ultrafine grain size, low initial defect density, and produced good contrast ideal for examining defect evolution. Samples were irradiated at nominally room temperature using a JEOL single-tilt stage, while video was collected at 6 and 15 frames per second for both Au *in situ* ion irradiation studies and Si *in situ* ion irradiation study, respectively.

The series of micrographs in Fig. 6 shows the effects of individual 48 MeV Si^{8+} ion strikes in a grain of Au oriented near a $\langle 011 \rangle$ zone axis under an ion flux of 6.7×10^9 Si^{8+} cm^{-2} s^{-1}. Defect clusters from Si ions were relatively small, with a few larger cascades appearing. Single ion events mostly produced compact defect clusters approximately 10–25 nm in diameter (noted by red arrows), while the largest observed were around 50 nm in diameter. Most defect clusters did not change from their initial appearance, and those that changed did so in less than 1 s. Counting the visible clusters in the observed area gives a dose rate of 2.6×10^7 Si^{8+} cm^{-2} s^{-1}, a discrepancy of more than 2 orders of magnitude. This difference can be explained by the TRIM simulation results discussed in Section 4; Si ions at this energy are subjected to relatively little nuclear stopping, and exit the thin foil, while producing only about 20 vacancies per ion. Thus many Si ions did not produce enough damage to be visible in the TEM.

In contrast, irradiation with 3.6 MeV Au^{6+} resulted in mostly large cascades containing multiple isolated defect structures spread up to hundreds of nm, with small ion tracks being the minority (Fig. 7). Note the difference in magnification between Figs. 6 and 7. The defect structure outlined in Fig. 7B was produced by a single ion event, and includes several discrete defect clusters, each approximately 25 nm in diameter. Again, defects remained static for the most part, although some changes in structure were observed when clusters from new cascades overlapped with existing defects. The ion flux measured by counting cascade events within the viewing area was 8.8×10^7 Au^{6+} cm^{-2} s^{-1}, in much clo-
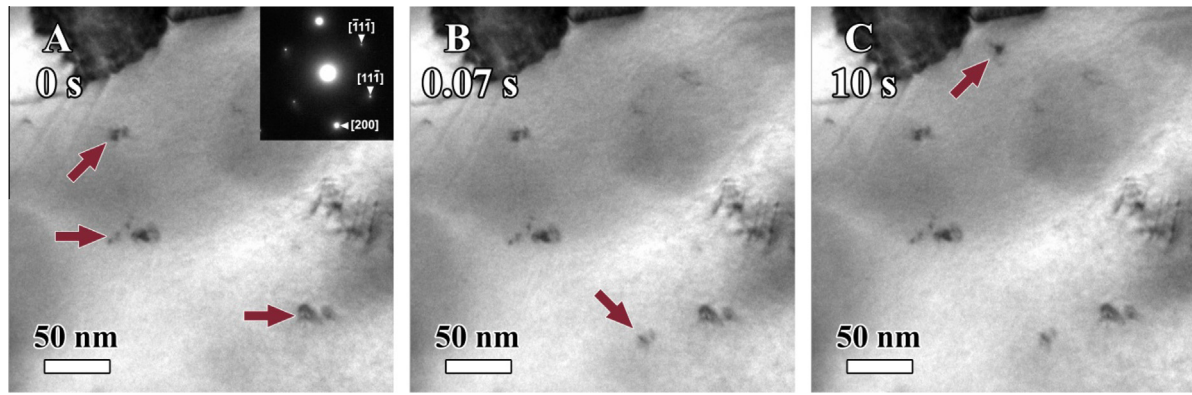
Fig. 6. Still frames from *in situ* video during 48 MeV Si^{8+} irradiation into Au at an ion flux of approximately 6.7×10^9 Si^{8+} cm^{-2} s^{-1}. (A) The inset selected area diffraction (SAD) pattern shows the large grain was near a $\langle 011 \rangle$ zone axis, while red arrows indicate three existing defect clusters. (B) Within one frame (nominally 0.07 s), a new defect cluster appeared (red arrow). (C) Several seconds later a similar event occurred again (red arrow). (For interpretation of the references to color in this figure legend, the reader is referred to the web version of this article.)
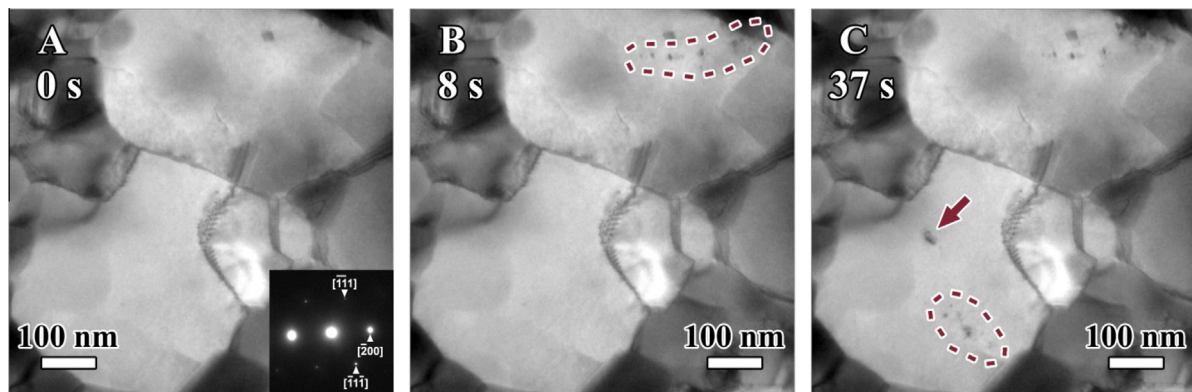

Fig. 7. Still frames from video collected *in situ* during 3.6 MeV Au^{6+} irradiation into Au at an ion flux of approximately 2.1×10^8 Au^{6+} cm^{-2} s^{-1}. (A) The microstructure before irradiation. The SAD pattern shows that the large grains were near a $\langle 011 \rangle$ zone axis. (B) The dotted red lines show the extent of the remnant defects from a single collision cascade. (C) The red arrow shows defects from a smaller collision event ($t \sim 11$ s), while dotted red lines show the remnants of a third cascade immediately after appearing. (For interpretation of the references to color in this figure legend, the reader is referred to the web version of this article.)

ser agreement with the ion current computed from the Faraday cup (2.1×10^8 Au^{6+} cm^{-2} s^{-1}) than in the 48 MeV Si^{8+} ion beam case. Au ions at this energy experience much greater nuclear stopping and produce approximately 4500 vacancies per ion, and thus a greater density of visible defect clusters.

As mentioned previously, the motivation for applying multiple beams at once was to study synergistic effects of different ion species and energies. The defect clusters produced during irradiation by single beams in Figs. 6 and 7 typically appeared rapidly and remained static. After their initial abrupt appearance, some defect structures evolved over a few seconds. Some remained stable but moved a few nm from their initial position, while some clusters disappeared, suggesting recombination or escape from the foil surfaces. Significant changes regularly occurred when damage from a second cascade overlapped existing defects loops and stacking-fault tetrahedra. In contrast, irradiation by concurrent 3.6 MeV Au^{6+} and 10 keV He^{1+} beams from the Tandem and Colutron produced more dynamic defect behavior. Recombination or escape of defects from the surface was observed more frequently, and while some events still occurred immediately after the appearance of the clusters, others occurred after tens of seconds. Fig. 8A–C illustrates oscillatory movement of a dislocation loop produced from an Au cascade. The graph in Fig. 8D shows the loop position as a function of time. Similar behavior was observed by Arakawa

et al., before in α-Fe [52], and was attributed to stress-free 1-D Brownian motion. This behavior has been postulated to be important to the behavior of nuclear materials, as it affects the mobility of radiation-induced defects. The authors noted a temperature dependence of the motion, and hypothesized that interstitial impurities trap and release loops. The results here are interesting in that they include a dynamic local environment that changes constantly due to the introduction of implanted He atoms and associated point defects. This resulted in movement at lower temperatures and, as shown in Fig. 8D, oscillatory motion followed by a long period of static behavior, followed by a second period of oscillatory motion. Further work is needed to fully understand the role that the continuous He beam plays in this behavior.

In addition to these three examples, a few other initial experiments highlighting the capabilities of this facility have been published elsewhere. Li et al. showed that 3 MeV Cu^{3+} irradiation of an incoherent twin boundary in Cu at room temperature did not result in a denuded zone, but in contrast produced truncated stacking fault tetrahedra along the grain boundary [53]. Synergistic effects of He implantation and self-ion irradiation of an Au thin foil were demonstrated by Chisholm et al. In that study, the formation of He bubbles was found to occur earlier during concurrent experiments than in either set of sequential experimental conditions [54]. Recently, the effects of He implantation and heavy ion
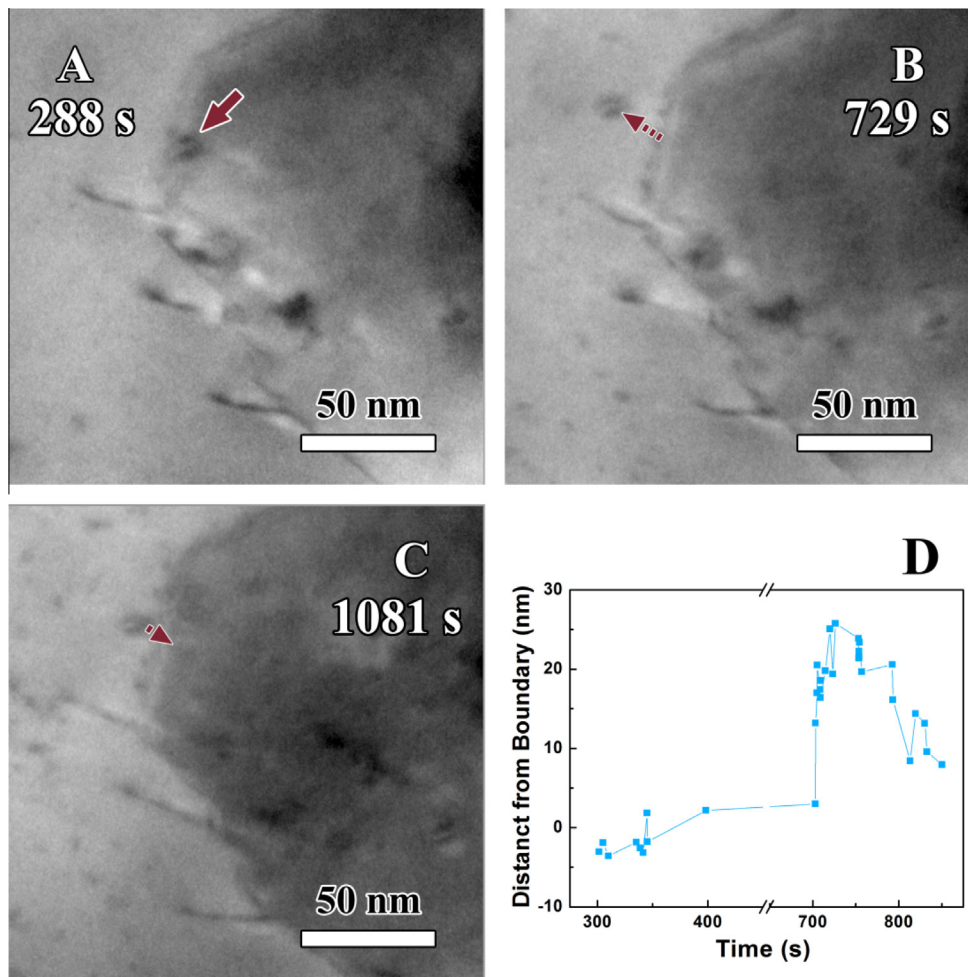
Fig. 8. Still frames from video collected *in situ* during concurrent 3.6 MeV Au^{6+} (4.3 × 10^9 Au^{6+} cm^{-2} s^{-1}) and 10 keV He^{1+} (2.4 × 10^{13} He^{1+} cm^{-2} s^{-1}) irradiation into Au foil. (A) The red arrow indicates a dislocation loop created by a single Au cascade residing near a long dislocation line. (B, C) Over time, the loop moved back and forth several nm, as indicated by the dotted red arrows. (D) Loop position as a function of time. (For interpretation of the references to color in this figure legend, the reader is referred to the web version of this article.)

irradiation of Au nanoparticles were studied by Bufford et al. [50]. In this work, both the radiation tolerance of standard nanoparticles and feasibility of producing far-from-equilibrium nanostructures were probed. The nanoparticle work also demonstrated the feasibility of combining *in situ* ion irradiation TEM with sequential electron tomography providing greater insight into the three-dimension evolution of the nanoparticles. The combination of results referenced and presented in this manuscript highlight the range of radiation environments that can be produced in the I^{3}TEM facility at Sandia National Laboratories.

In order to further improve the facility, work is continuously underway to enhance the capabilities to best emulate different aspects of extreme environments of interest, including temperature, atmosphere, loading parameters, and irradiation conditions. This work includes efforts to produce a greater number of overlapping *in situ* TEM conditions, improve the temporal resolution, produce greater temperature control of the TEM sample, increase the range of beam species and energies, and enhance control of the ion beams.

8. Summary

An *in situ* ion irradiation transmission electron microscope (I^{3}TEM) at the Ion Beam Laboratory of Sandia National Laboratories has been developed and is operational. This facility permits both

high-energy ion irradiation and low-energy gas ion implantation of electron transparent samples during real time TEM observation, while maintaining the factory 2.5 Å point resolution during many experiments. Ion beams used successfully to date span an energy range from 48 MeV Si^{8+} to 10 keV He$^+$, at ion fluxes ranging from 1.6 × 10^7 to 3.2 × 10^{13} ions cm^{-2} s^{-1}. Samples can be subjected to *in situ* heating and mechanical loading during irradiation, and tomography and photon optics provide further means to investigate specimens. This facility also permits both *in situ* and *ex situ* concurrent dual beam exposure, as has been demonstrated here with 10 keV He$^+$ and 3.6 MeV Au^{6+}ion beams bombarding polycrystalline Au foils. The current capabilities of this facility are being applied to a wide range of material systems to understand microstructural response of the materials in various and overlapping extreme environments.

assistance in the development of this facility. This work was partially supported by the US Department of Energy, Office of Basic Energy Sciences. Sandia National Laboratories is a multi-program laboratory managed and operated by Sandia Corporation, a wholly owned subsidiary of Lockheed Martin Corporation, for the U.S. Department of Energy's National Nuclear Security Administration under contract DE-AC04-94AL85000.

Appendix A. Supplementary data

Supplementary data associated with this article can be found, in the online version, at http://dx.doi.org/10.1016/j.nimb.2014.08.002.

References

[1] B.D. Wirth, How does radiation damage materials?, Science 318 (5852) (2007) 923–924
[2] Integrated Computational Materials Engineering: A Transformational Discipline for Improved Competitiveness and National Security, The National Academies Press, 2008.
[3] B. Cox, Some thoughts on the mechanisms of in-reactor corrosion of zirconium alloys, J. Nucl. Mater. 336 (2–3) (2005) 331–368.
[4] P.R. Okamoto, L.E. Rehn, Radiation-induced segregation in binary and ternary alloys, J. Nucl. Mater. 83 (1) (1979) 2–23.
[5] T. Tanaka et al., Synergistic effect of helium and hydrogen for defect evolution under multi-ion irradiation of Fe–Cr ferritic alloys, J. Nucl. Mater. (2004) 329–333 (Part A (0): pp. 294–298).
[6] G. Vizkelethy et al., Radiation effects microscopy for failure analysis of microelectronic devices, Nucl. Instr. Meth. Phys. Res. B Beam Interact. Mater. Atoms 231 (2005) 467–475.
[7] J.R. Schwank, M.R. Shaneyfelt, P.E. Dodd, Radiation hardness assurance testing of microelectronic devices and integrated circuits: radiation environments, physical mechanisms, and foundations for hardness assurance, IEEE Trans. Nucl. Sci. 60 (3) (2013) 2074–2100.
[8] E. Ruska, The development of the electron-microscope and of electron-microscopy, Rev. Mod. Phys. 59 (3) (1987) 627–638.
[9] L. Marton, A new electron microscope, Phys. Rev. 58 (1) (1940) 57–60.
[10] J. Hillier, A.W. Vance, Recent developments in the electron microscope, Proc. IRE 29 (4) (1941) 167–176.
[11] D.W. Pashley, A.E.B. Presland, Ion damage to metal films inside an electron microscope, Philos. Mag. 6 (68) (1961) 1003–1012.
[12] M.K. Hossain, L.M. Brown, Electron irradiation damage in magnesium, Acta Metall. 25 (3) (1977) 257–264.
[13] E.P. Butler, In situ experiments in the transmission electron-microscope, Rep. Prog. Phys. 42 (5) (1979) 833–895.
[14] J.A. Hinks, A review of transmission electron microscopes with in situ ion irradiation, Nucl. Instr. Meth. Phys. Res. B Beam Interact. Mater. Atoms 267 (23–24) (2009) 3652–3662.
[15] M.A. Kirk et al., The collapse of defect cascades to dislocation loops, J. Nucl. Mater. 149 (1) (1987) 21–28.
[16] M.A. Kirk, Production of defects in metals by collision cascades: TEM experiments, in: I.M. Robertson, et al. (Eds), Microstructure of Irradiated Materials, 1995. pp. 47–56.
[17] Y. Serruys et al., JANNUS: a multi-irradiation platform for experimental validation at the scale of the atomistic modelling, J. Nucl. Mater. 386–88 (2009) 967–970.
[18] J.A. Hinks, J.A. van den Berg, S.E. Donnelly, MIAMI: microscope and ion accelerator for materials investigations, J. Vacuum Sci. Technol. A 29 (2) (2011).
[19] T. Takeyama, S. Ohnuki, H. Takahashi, Study of cavity formation in 316 stainless steels by means of HVEM/ion-accelerator dual irradiation, J. Nucl. Mater. 133–134 (1985) 571–574.
[20] H. Abe et al., The TEM-Accelerators Facility at JAERI-Takasaki and its Application to Materials Science, Japan Atomic Energy Research Institute, 1996.
[21] S. Ishino, A review of in situ observation of defect production with energetic heavy ions, J. Nucl. Mater. 251 (1997) 225–236.
[22] K. Hattar et al., Length scale effect on deformation and failure mechanisms of ultra-fine grained aluminum, MRS Online Proc. Libr. 907 (2005). 0907-MM01-03.
[23] R.C. Hugo et al., In-situ TEM tensile testing of DC magnetron sputtered and pulsed laser deposited Ni thin films, Acta Mater. 51 (7) (2003) 1937–1943.
[24] K. Jagannadham, H.G.F. Wilsdorf, J. Weertman, Dislocations at ductile/plastic crack tips: in-situ TEM observations, Mater. Res. Innovations 1 (4) (1998) 254–264.
[25] D. Caillard, Kinetics of dislocations in pure Fe. Part I. In situ straining experiments at room temperature, Acta Mater. 58 (9) (2010) 3493–3503.
[26] A. Couret et al., In-situ deformation in TEM – recent developments, Microsc. Microanal. Microstruct. 4 (2–3) (1993) 153–170.
[27] J.T.M. De Hosson et al., In situ TEM nanoindentation and dislocation-grain boundary interactions: a tribute to David Brandon, J. Mater. Sci. 41 (23) (2006) 7704–7719.
[28] R.D. Field, P.A. Papin, Location specific in situ TEM straining specimens made using FIB, Ultramicroscopy 102 (1) (2004) 23–26.
[29] G.M. Bond, I.M. Robertson, H.K. Birnbaum, On the determination of the hydrogen fugacity in an environmental cell tem facility, Scr. Metall. 20 (5) (1986) 653–658.
[30] R.C. Hugo, R.G. Hoagland, Gallium penetration of aluminum: in-situ TEM observations at the penetration front, Scripta Mater. 41 (12) (1999) 1341–1346.
[31] F.M. Ross, Growth processes and phase transformations studied in situ transmission electron microscopy, IBM J. Res. Dev. 44 (4) (2000) 489–501.
[32] P.L. Gai, R. Sharma, F.M. Ross, Environmental (S) TEM studies of gas–liquid–solid interactions under reaction conditions, MRS Bull. 33 (02) (2008) 107–114.
[33] N. de Jonge, W.C. Bigelow, G.M. Veith, Atmospheric pressure scanning transmission electron microscopy, Nano Lett. 10 (3) (2010) 1028–1031.
[34] L. Sun et al., In situ transmission electron microscopy observation of silver oxidation in ionized/atomic gas, Langmuir 27 (23) (2011) 14201–14206.
[35] N.M. Boyall, K. Durose, I.M. Watson, An in-situ TEM-cathodoluminescence study of electron beam degradation of luminescence from GaN and In0.1Ga0.9N quantum wells, in: C. Wetzel, et al. (Eds.), Gan and Related Alloys-2002, 2003, pp. 683–688.
[36] P.A. Midgley, R.E. Dunin-Borkowski, Electron tomography and holography in materials science, Nat. Mater. 8 (4) (2009) 271–280.
[37] R.F. Egerton, Analytical electron microscopy, in: Physical Principles of Electron Microscopy, Springer, New York, NY, 2005, pp. 155–175.
[38] G. Botton, Analytical electron microscopy, in: P.W. Hawkes, J.C.H. Spence (Eds.), Science of Microscopy, Springer, New York, NY, 2007, pp. 273–405.
[39] K. Al-Fadhalahy et al., Modeling texture evolution during rolling of a Cu–Nb multilayered system, Phil. Mag. 85 (13) (2005) 1419–1440.
[40] G. Vizkelethy, B.L. Doyle, F.L. McDaniel, The new Sandia light ion microbeam, Nucl. Instr. Meth. Phys. Res. B Beam Interact. Mater. Atoms 273 (2012) 222–225.
[41] F.D. McDaniel, et al., The tandem-RFQ linac booster at Sandia national laboratories, in: J.L. Duggan, I.L. Morgan (Eds.), Application of Accelerators in Research and Industry, 2003, pp. 986–990.
[42] R. Middleton, A Negative Ion Cookbook, University of Pennsylvania, Philadelphia, PA, 1990.
[43] B.L. Doyle, D.K. Brice, W.R. Wampler, Hydrogen in fusion first wall surfaces, Nucl. Sci. IEEE Trans. 28 (2) (1981) 1299–1303.
[44] W.R. Wampler, C.W. Magee, Depth resolved measurements of hydrogen isotope exchange in carbon, J. Nucl. Mater. 103 (1–3) (1982) 509–512.
[45] W.E. Frahn, W.L. Rautenbach, L. Wåhlin, The electromagnetic isotope separator in Pretoria, Nucl. Instr. Meth. 7 (3) (1960) 253–268.
[46] L. Wåhlin, The Colutron Mark II, a velocity filter isotope separator, Nucl. Instr. Meth. 38 (1965) 133–139.
[47] J.F. Ziegler, M.D. Ziegler, J.P. Biersack, SRIM – the stopping and range of ions in matter (2010), Nucl. Instr. Meth. Phys. Res. B Beam Interact. Mater. Atoms 268 (11–12) (2010) 1818–1823.
[48] S.M. Hoppe et al., In-situ transmission electron microscopy of liposomes in an aqueous environment, Langmuir (2013).
[49] P.J. Cappillino et al., Synthesis of mesoporous palladium with tunable porosity and demonstration of its thermal stability by in situ heating and environmental transmission electron microscopy, J. Mater. Chem. A 1 (3) (2013) 602–610.
[50] D. Bufford et al., In situ TEM ion irradiation and implantation effects on Au nanoparticle morphologies, Chem. Commun. 50 (57) (2014) 7593–7596.
[51] K. Hattar et al., Defect structures created during abnormal grain growth in pulsed-laser deposited nickel, Acta Mater. 56 (4) (2008) 794–801.
[52] K. Arakawa et al., Observation of the one-dimensional diffusion of nanometer-sized dislocation loops, Science 318 (5852) (2007) 956–959.
[53] N. Li, K. Hattar, A. Misra, In situ probing of the evolution of irradiation-induced defects in copper, J. Nucl. Mater. 439 (1–3) (2013) 185–191.
[54] C. Chisholm, A. Minor, K. Hattar, In situ TEM concurrent and successive Au self-ion irradiation and He implantation, Mater. Trans. 55 (3) (2014) 418–422.